J Mater Sci (2017) 52:13561–13571

Energy materials

Hydrothermal synthesis of N-doped RGO/$MoSe_2$ composites and enhanced electro-catalytic hydrogen evolution

Long Zhang[1], Lan Sun[1], Yuhong Huang[2], Yunjin Sun[3], Tingwei Hu[1], Kewei Xu[1,4,*], and Fei Ma[1,*]

[1] State Key Laboratory for Mechanical Behavior of Materials, Xi'an Jiaotong University, Xi'an 710049, Shaanxi, China
[2] College of Physics and Information Technology, Shaanxi Normal University, Xi'an 710062, Shaanxi, China
[3] Beijing Laboratory of Food Quality and Safety, Beijing University of Agriculture, Beijing 102206, China
[4] Department of Physics and Opt-electronic Engineering, Xi'an University of Arts and Science, Xi'an 710065, Shaanxi, China

Received: 24 April 2017
Accepted: 20 July 2017
Published online: 24 August 2017

ABSTRACT

A facile two-step hydrothermal approach is adopted to synthesize $MoSe_2$/N-doped RGO (NG) composites with the N/C atomic percentage changing from 1.13 to 5.16 at%. In the composites, nanoclusters of $MoSe_2$ nanosheets are dispersed on plicated NG nanosheets. The electrochemical measurement suggests that the $MoSe_2$/NG composites exhibit enhanced electro-catalytic HER activity as compared to $MoSe_2$ and $MoSe_2$/RGO. Moreover, as the N/C ratio of NG is increased, the activity of $MoSe_2$/NG increases firstly and then decreases. At low N/C ratio, the impact of interfacial energy barrier between $MoSe_2$ and NG is negligible and the electron transfer is substantial, so the activity of the $MoSe_2$/NG composites increases with carrier concentration in NG. However, at high N/C ratio, the energy barrier blocks the electron transfer from NG to $MoSe_2$ remarkably. Consequently, the $MoSe_2$/NG composites with an intermediate N/C ratio have the highest activity. Owing to the synergistic effect of NG and $MoSe_2$, the Tafel slope of the composites is reduced from 114.69 to 78.45 mV dec^{-1} by 32% as compared to pure $MoSe_2$. The results provide us valuable information for efficient design of transition metal dichalcogenide catalysts for electro-catalytic hydrogen evolution.

Introduction

With growing population and expanding industrialization in the world, the demands for energy have been promptly increased in recent years [1]. To date, gigantic consumption of fossil fuel seriously threatens the environmental security. So it is quite urgent to develop eco-friendly energy sources replacing fossil fuels. Hydrogen energy is believed to be one of promising clean and renewable energies [2–4],

Address correspondence to E-mail: kwxu@mail.xjtu.edu.cn; mafei@mail.xjtu.edu.cn

DOI 10.1007/s10853-017-1417-7

Electro-catalytic hydrogen evolution reaction (HER) is an effective method to produce hydrogen with high efficiency [5]. Platinum (Pt) has been proved to be state-of-the-art catalyst for electro-catalytic HER, but the large-scale application is limited by its extremely high cost [6–8]. It is very necessary to explore cheap and efficient electro-catalysts.

$MoSe_2$ is a typical transition metal dichalcogenides (TMDs) with lamellar structure in which each Se-Mo-Se sandwiched layer is held together by van der Waals interaction [9]. Few-layer counterparts can be fabricated by hydrothermal method [10], mechanical exfoliation [11] and chemical vapor deposition (CVD) [12, 13]. Recently, it was found that $MoSe_2$ might be a promising electro-catalyst for HER, and the unsaturated Se edges in $MoSe_2$ are electro-catalytically active [14, 15]. According to the DFT calculations, the hydrogen binding energy at S/Se edges of MoS_2 and $MoSe_2$ is −34.6 and −13.1 meV/f.u., respectively. So the binding of hydrogen atoms on Se edge is weaker than that on S edge, and thus a higher exchange current for hydrogen evolution was predicted for $MoSe_2$ [17]. Moreover, the Fermi energy (E_F) of $MoSe_2$ is more close to the normal hydrogen electrode with respect to MoS_2. As a result, 2H–$MoSe_2$ is more active than 2H–MoS_2 for HER, which was proved by the HER experiments [16, 17]. However, the electrical conductivity of both $MoSe_2$ and MoS_2 is not good, which restricts their activity to some degree [18, 19]. As well known, graphene sheets possess good electrical conductivity and very large specific surface area. If $MoSe_2$ or MoS_2 are dispersed on graphene sheets, their conductivity should be significantly improved. So graphene sheets are regarded as the ideal support [19–23]. Since N-doping can effectively regulate the electronic states and chemical features, N-doped RGO (NG) as one of the derivatives of graphene usually exhibits better performance than graphene [24, 25] and has attracted intensive attention. For instance, pyrrolic nitrogen atoms in graphene lattice were proved to be effective to activate and reduce the oxygen molecules in oxygen reduction reaction (ORR), that is, N-doping might regulate the electronic states and chemical properties of graphene [26]. In addition, NG was also regarded to be promising in HER, because nitrogen atoms in NG have strong interaction with H^+ for HER [25]. For example, CdS/NG hybrid structure showed enhanced catalytic activity for H_2 evolution. The doped N facilitates the reaction kinetics of HER, and further substantially improves the activity [27]. Similar effects have been reported in other systems, such as, Fe_2P/NG nanocomposites and MoS_2/NG hybrid [28, 29]. But the optimal N component and the mechanism is not well known.

In this paper, a facile two-step hydrothermal approach is adopted to synthesize $MoSe_2$/NG composites with N/C ratio changing from 1.13 to 5.16 at%. It is expected that NG in the composites act as a channel for electron transfer, and the electronic states and conductivity are regulated by changing the atomic ratio of N/C. X-ray photoelectron spectroscopy (XPS), X-ray diffraction (XRD), Raman spectra, field emission scanning electron microscopy (FESEM) and high-resolution transmission electron microscopy (HRTEM) are used to characterize the structures of $MoSe_2$/NG composites. The dependence of electro-catalytic activity on the carrier concentration in NG is studied, and the influence on the HER performance is discussed in details.

Experimental

Synthesis of samples

Chemical reagents

All chemical reagents, including graphite powders, sodium nitrate ($NaNO_3$), sulfuric acid (H_2SO_4, 98%), potassium permanganate ($KMnO_4$), hydrogen peroxide (H_2O_2, 30%), sodium molybdate dihydrate ($Na_2MoO_4{\cdot}2H_2O$), hydrazine hydrate ($N_2H_4{\cdot}H_2O$, 85%), selenium powder (Se), ammonia solution ($NH_3{\cdot}H_2O$, 30%), are analytical grade and are used without further purification.

Synthesis of NG

Firstly, the GO sheets were fabricated from graphite powders by the modified Hummer's method [30]. Then 15 mg GO was dispersed into 30 mL distilled water with magnetic stirring for 5 min and with sonication for 1 h, and 100 μL 30% ammonia solution as the nitrogen source was added into the above solution. Subsequently, different amount of $N_2H_4{\cdot}H_2O$ was introduced to adjust the atomic ratio of N/C. Finally, the homogeneous solution was transferred into a 50-mL Teflon-lined autoclave and kept at 160 °C for 6 h. The precipitates were collected,

washed by distilled water three times and by ethanol two times, and then dried at 80 °C in a vacuum oven overnight to prepare four NG samples, NG1, NG2, NG3, and NG4. The atomic ratio of N/C was measured by XPS spectra.

Synthesis of $MoSe_2$/NG

Five milligrams of as-synthesized NG was dispersed into 10 mL distilled water with magnetic stirring for 5 min and with sonication for 1 h, then 0.484 g $Na_2MoO_4{\cdot}2H_2O$ was added into the solution with stirring for another 5 min to form uniform solution. 0.316 g Se powder was dissolved into 5 ml hydrazine hydrate and maintained in another 10-mL flask for 24 h. Finally, the mixed solution was transferred into 50-mL Teflon-lined autoclave and kept at 220 °C for 12 h. The precipitates were collected, washed by distilled water three times and by ethanol two times, and dried at 80 °C in a vacuum oven overnight. $MoSe_2$/RGO composites and pure $MoSe_2$ were also prepared for comparison. To this end, RGO rather than NG was adopted in the above preparation route and pure $MoSe_2$ in absence of NG.

Microstructure characterization

XRD (SHIMADZU XRD-7000S diffractometer) was adopted to analyze the phase structure of the as-prepared samples. FESEM (FEI Quanta 600S) and HRTEM (JEOL JEM 2100F) were adopted to characterize the morphology and microstructure of the samples. N_2 adsorption–desorption isotherms were measured on Micromeritics ASAP2020. The specific surface areas were determined by the Brunauer–Emmett–Teller (BET) method. Raman spectra were examined by a Horiba HR800 spectrometer with a 633-nm laser as the excitation light source. XPS measurements were performed on Thermo Scientific K-Alpha XPS spectrometer, and the binding energies were corrected by referencing the peak of C 1s at 284.80 eV. PL spectra were detected with a PTI QM40 spectrometer using a 532-nm line from a Xenon lamp.

Electrochemical evaluation

One milligram of catalysts ($MoSe_2$/NG, $MoSe_2$/RGO, and $MoSe_2$) was suspended in solution containing 400 μL ethanol and 10 μL of 5% nafion solution by sonication for 40 min. Then the uniform inks were drop-casted on carbon fiber paper (CFP) with the electrode area of 1 cm^2 and dried in air for 12 h. The electrochemical experiments were done in an Autolab PGSTAT 128 N station via a standard three-electrode configuration. The CFP electrode was adopted as the working electrode, and a graphite rod and Ag/AgCl were used as counter and reference electrodes, respectively. Pt/C with the same amount of $MoSe_2$/NG loaded on the CFP was also used as working electrode for comparison. The Ag/AgCl reference electrode was calibrated to be −0.226 V (vs. RHE) by $E(\mathrm{RHE}) = E(\mathrm{Ag/AgCl}) + 0.197 + 0.059\ \mathrm{pH}$. The electro-catalysis was measured using linear sweep voltammetry (LSV) from 0.2 to −0.5 V (vs. RHE) with a scanning rate of 5 mV/s in 0.5 M H_2SO_4. The electrochemical impedance spectroscopy (EIS) was measured in the frequency range from 100 kHz to 1 Hz centered at −0.2 V (vs. RHE) with an amplitude of 10 mV. The Ohmic loss in all the data (except for EIS) was corrected. The Nyquist plots were employed to fit the *Rs* of $MoSe_2$, $MoSe_2$/RGO, $MoSe_2$/NG1, $MoSe_2$/NG2, $MoSe_2$/NG3, $MoSe_2$/NG4, and the values were 1.30, 1.57, 1.49, 1.67, 1.64, and 1.53 Ω, respectively. Cyclic voltammetry (CV) was used to measure the electrochemical double-layer capacitance at non-Faradaic potential and to estimate the effective electrode surface area. The scan rates are 10, 20, 50, 100, and 200 mV s^{-1}. The stability of electrocatalysts was examined by continuous cycling between 0 V and −0.4 V (vs. RHE) at a scanning rate of 100 mV s^{-1} for 1000 cycles. Before measurement, the electrolyte was deaerated with high-purity N_2 for 30 min.

Results and discussion

Figure 1a shows the XPS spectra of the NG samples. The peaks at 284.8 and 400.3 eV can be assigned to the binding energies of C 1s and N 1s. Figure 1b–e displays the high-resolution XPS (HR-XPS) spectra of N 1s. Evidently, nitrogen dopants have been successfully introduced into the samples; moreover, the N 1s peak is enhanced gradually from samples NG1 to NG4, indicating the increased N component. The atomic percentage of N/C in NG1, NG2, NG3, and NG4 is 1.13, 1.94, 3.0, and 5.16 at%, respectively, and the results are listed in Table 1. The HR-XPS peak of N 1s can be resolved into three peaks at 398.4, 400.1, and 401.3 eV corresponding to pyridinic-N, pyrrolic-N, and graphitic-N, respectively, [31] as listed in

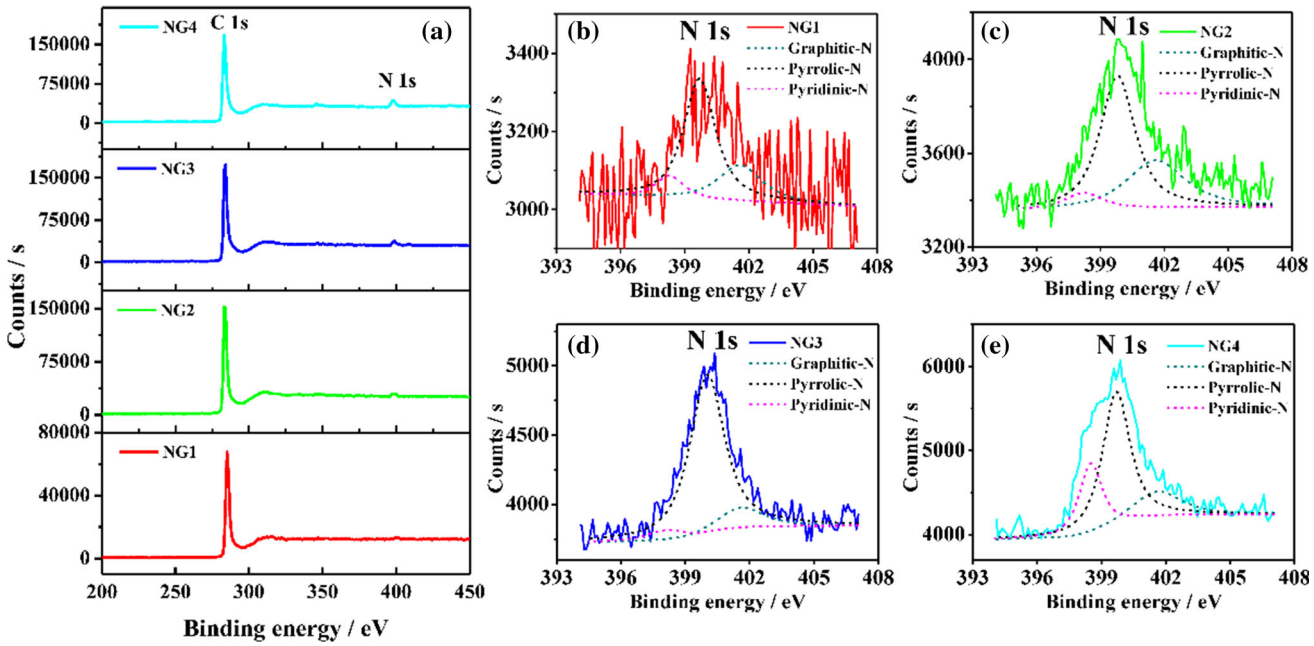

Figure 1 **a** XPS spectrum of NG; HR-XPS spectrum of N in **b** NG1, **c** NG2, **d** NG3, **e** NG4.

Table 1 Nitrogen atomic percentage, η_{50}, Tafel slope, and fitting results of Nyquist plots in $MoSe_2$, $MoSe_2$/RGO and $MoSe_2$/NG

Samples	N/C (%)	N			η_{50} (V vs. RHE)	Tafel slope (mV dec^{-1})	R_s (Ω)	R_{ct} (Ω)
		Pyridinic-N (%)	Pyrrolic-N (%)	Graphitic-N (%)				
$MoSe_2$	–	–	–	–	−0.417	114.69	1.30	14.46
$MoSe_2$/RGO	–	–	–	–	−0.345	90.87	1.57	10.68
$MoSe_2$/NG1	1.13	10.42	63.51	26.07	−0.332	82.36	1.49	9.41
$MoSe_2$/NG2	1.94	8.10	57.59	34.31	−0.294	78.45	1.67	6.82
$MoSe_2$/NG3	3.00	6.15	80.54	13.31	−0.323	84.06	1.64	8.24
$MoSe_2$/NG4	5.16	24.91	55.87	19.22	−0.327	81.57	1.53	9.30

Table 1. More than 50% N exists in the formation of pyrrolic-N, about 20% in graphitic-N, and 10% in pyridinic-N. The pyridinic-N in NG sheets might result in new electronic states at Fermi level and improve the electric conductivity [32].

Figure 2 shows the XRD patterns of the as-synthesized $MoSe_2$, $MoSe_2$/RGO, and $MoSe_2$/NG composites. The diffraction peaks of $MoSe_2$ can be perfectly indexed to the (002), (100), (103), (105), and (110) planes of hexagonal 2H-$MoSe_2$ (JCPDS 29-0914) [33]. However, no diffraction peak of RGO or NG is observed in $MoSe_2$/RGO and $MoSe_2$/NG composites, and the peaks of composites are similar to those in pure $MoSe_2$. It indicates that the RGO or NG is not well stacked during the hydrothermal process [34], and RGO and NG affect the growth of $MoSe_2$ nanosheets little. The broad diffraction peaks suggest nanosize feature of $MoSe_2$ sheets [10]. The full width at half maximum (FWHM) of diffraction peaks of $MoSe_2$/RGO and $MoSe_2$/NG composites is listed in Table S1[Electronic Supplementary Information], and it is slightly larger than that of pure $MoSe_2$ owing to the lowered crystallinity in the composites since RGO and NG sheets promote the nucleation and thus reduce the size of $MoSe_2$ nanosheets.

Figure 3 shows the Raman spectra of the samples. The Raman peaks at 237 and 281 cm^{-1} are from the out-of-plane A_{1g} and in-plane E^1_{2g} vibration modes in hexagonal $MoSe_2$ [10] In all the samples, the intensity of E^1_{2g} mode is lower than that of A_{1g} mode, characteristics of edge-rich feature in $MoSe_2$ nanosheets

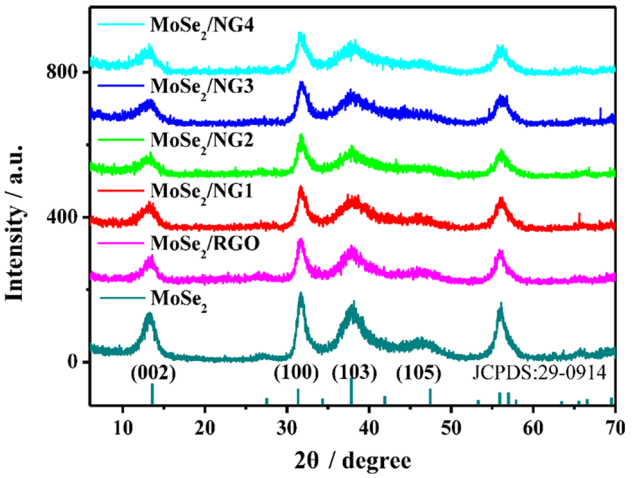

Figure 2 XRD patterns of as-prepared $MoSe_2$, $MoSe_2$/RGO and $MoSe_2$/NG.

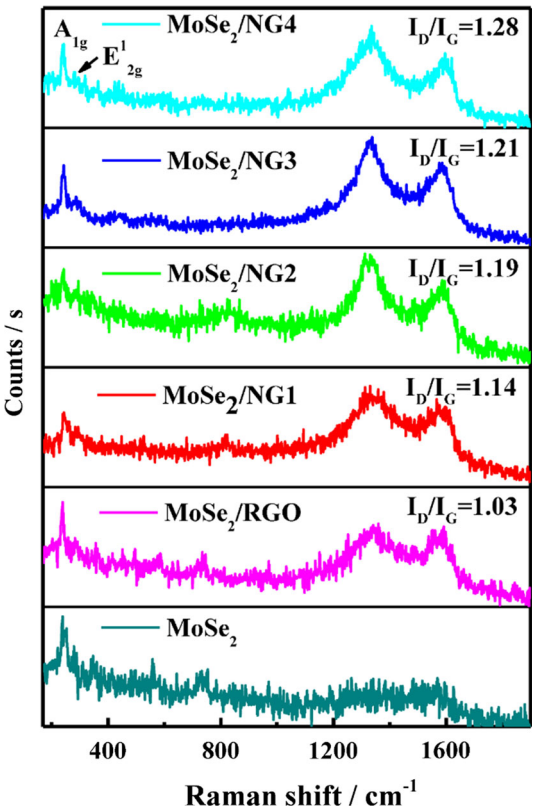

Figure 3 Raman spectra of as-prepared $MoSe_2$, $MoSe_2$/RGO and $MoSe_2$/NG.

[35]. The peaks at 1334 and 1584 cm^{-1} corresponding to the D- and G-bands of graphene can be identified from the spectra of $MoSe_2$/RGO and $MoSe_2$/NG samples [36, 37]. So the $MoSe_2$/RGO and $MoSe_2$/NG composites are successfully fabricated via a two-step hydrothermal method. The intensity ratio of I_D/I_G was usually adopted to evaluate the structural disorder and defects in graphene [38–40]. The I_D/I_G ratio of $MoSe_2$/RGO, $MoSe_2$/NG1, $MoSe_2$/NG2, $MoSe_2$/NG3, and $MoSe_2$/NG4 is determined as 1.03, 1.14, 1.19, 1.21, and 1.28, respectively. Obviously, the I_D/I_G ratio increases with the N/C ratio gradually, that is, N-doping leads to structural disorder in NG, which is consistent with the reported results [41].

Figures 4a–f displays the SEM images of pure $MoSe_2$, $MoSe_2$/RGO, $MoSe_2$/NG1, $MoSe_2$/NG2, $MoSe_2$/NG3 and $MoSe_2$/NG4, respectively. As shown in Fig. 4a, pure $MoSe_2$ exists in nanoclusters which are composed of nanosheets. The lamellar RGO and NG with plicated feature are clearly observed in $MoSe_2$/RGO and $MoSe_2$/NG composites; moreover, $MoSe_2$ nanoclusters are tightly intertwined with RGO and NG sheets. It is worth noting that the plicated feature becomes more remarkable in $MoSe_2$/NG composites, particularly, in the composites with the higher N/C ratio. N_2 adsorption–desorption isotherm curves are measured to evaluate the specific surface area of the as-prepared samples according to the BET method, and the results are displayed in Figure S1. The specific surface area of $MoSe_2$, $MoSe_2$/RGO, $MoSe_2$/NG1, $MoSe_2$/NG2, $MoSe_2$/NG3, and $MoSe_2$/NG4 is 22.4, 29.5, 34.2, 29.3, 32.2, and 31.8 $m^2\ g^{-1}$, respectively. Obviously, the composites have much larger specific surface area as compared to the pure $MoSe_2$. Taking the $MoSe_2$/NG3 composite as an example, Fig. 5a–c show the TEM and HRTEM images, and SAED patterns. It can be seen from Fig. 5a that the diameter of $MoSe_2$ nanoclusters is 120 ~ 150 nm. Ultra-thin NG3 sheets are distinguished from the TEM images. Lamellar structures with an interplanar spacing of 0.66 nm corresponding to (002) planes of $MoSe_2$ can be identified from the HRTEM image (Fig. 5b). The SAED patterns in Fig. 5c suggest that $MoSe_2$ in $MoSe_2$/NG3 sample is polycrystalline, and the diffraction rings correspond to (100), (103), and (110) planes of hexagonal 2H–$MoSe_2$, as shown in XRD patterns.

The electro-catalytic HER performance of $MoSe_2$, $MoSe_2$/RGO, and $MoSe_2$/NG is evaluated by using LSV. Commercial Pt/C catalyst on CFP is also examined for comparison. Ohmic resistance (*iR*) affects the intrinsic performance, Fig. 6a shows the LSV data after correction. Among all the samples, pure $MoSe_2$ samples exhibit the smallest current

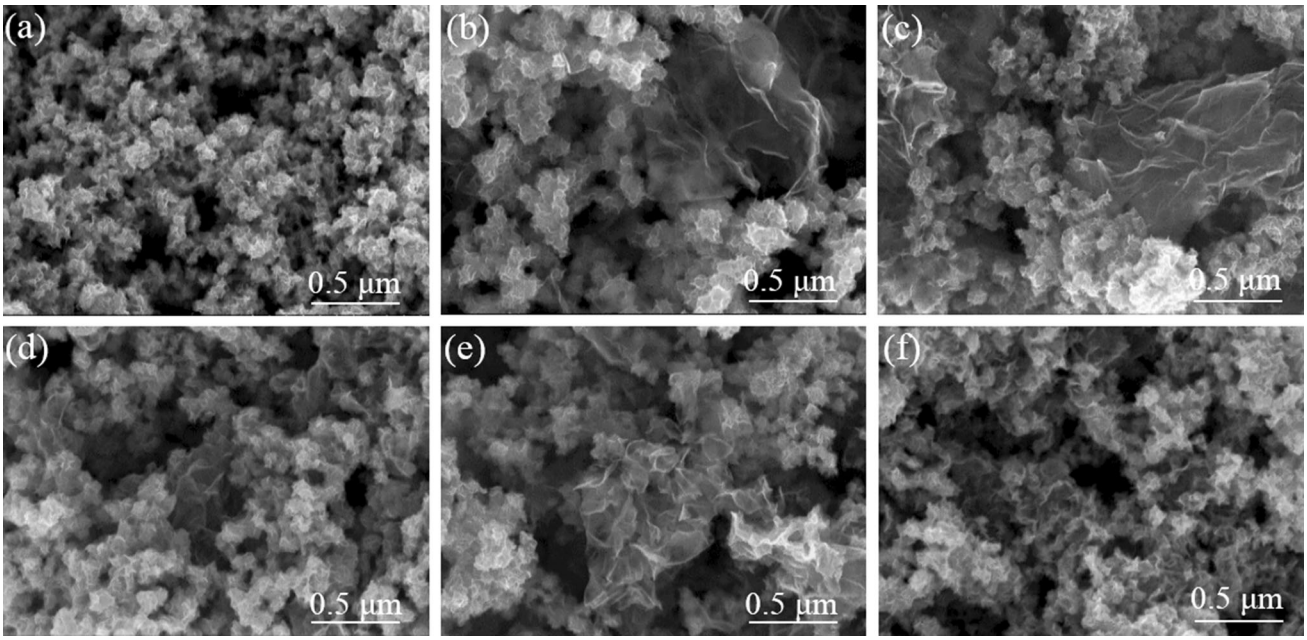

Figure 4 SEM images of the samples. **a** $MoSe_2$, **b** $MoSe_2$/RGO, **c** $MoSe_2$/NG1, **d** $MoSe_2$/NG2, **e** $MoSe_2$/NG3, **f** $MoSe_2$/NG4.

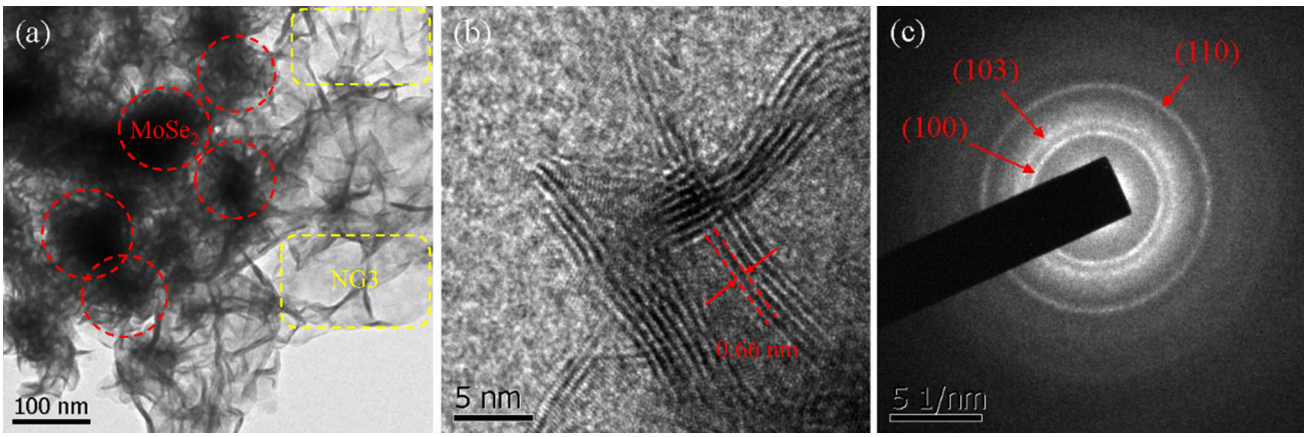

Figure 5 **a** TEM, **b** HRTEM, and **c** SAED patterns of $MoSe_2$/NG3 samples.

density, but the current density is substantially enhanced in $MoSe_2$/RGO and $MoSe_2$/NG composites. The overpotential required at a current density of 10 mA cm^{-2} (η_{10}) is usually regarded as a benchmark to evaluate the activity of HER catalysts. The η_{10} of $MoSe_2$/RGO, $MoSe_2$/NG1, $MoSe_2$/NG3, and $MoSe_2$/NG4 is lower than that of pure $MoSe_2$ (−0.261 V vs. RHE). In particular, $MoSe_2$/NG2 has the lowest η_{10} of −0.229 V (vs. RHE). To further check the activity of the samples, the overpotential required at a current density of 50 mA cm^{-2} (η_{50}) is measured, and the results are listed in Table 1. As compared to pure $MoSe_2$ (−0.417 V vs. RHE), the η_{50} of $MoSe_2$/RGO composites (−0.345 V vs. RHE) is lowered by 17%. That is, the synergistic effect of RGO and $MoSe_2$ improves the activity greatly. The η_{50} value of the $MoSe_2$/NG composites is further reduced. So N-doping into graphene could enhance the activity further. Notably, $MoSe_2$/NG2 exhibits the best activity owing to the smallest η_{50}. Tafel slope is an important parameter describing the HER performance [42]. The smaller Tafel slope corresponds to the lower overpotential required for an increased current density [43]. The Tafel plots are derived from the polarization curves, and the linear portion is fitted as following:

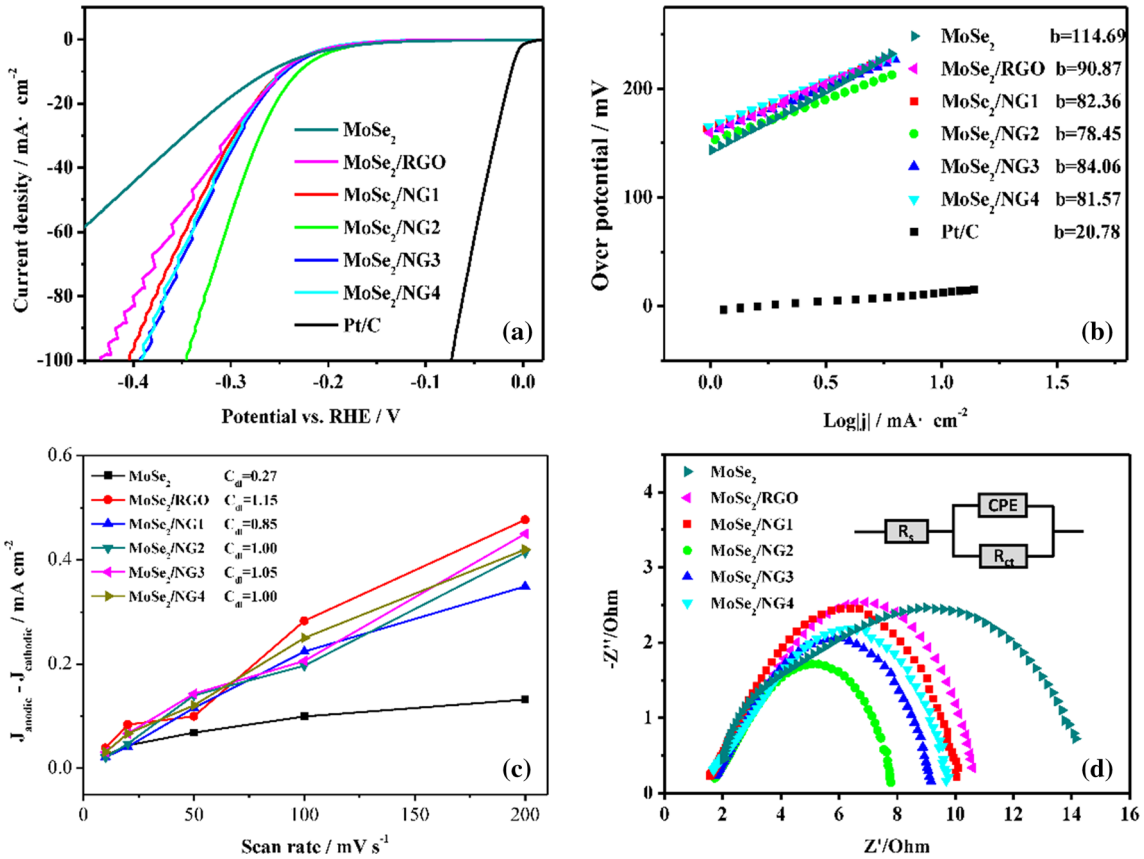

Figure 6 **a** Linear sweeping voltammetry, **b** Tafel plots, **c** Double-layer capacity currents versus scan rates, **d** Nyquist plots of $MoSe_2$, $MoSe_2$/RGO and $MoSe_2$/NG.

$$\eta = b \log j + a \quad (1)$$

in which η is the overpotential, j is the current density, and b is the Tafel slope [15]. As shown in Fig. 6b and Table 1, the Tafel slope of $MoSe_2$/RGO is calculated as 90.87 mV dec^{-1}, which is smaller than that of pure $MoSe_2$ (114.69 mV dec^{-1}) by 20%. The Tafel slope is further reduced to 82.36, 78.45, 84.06, and 81.57 mV dec^{-1} for $MoSe_2$/NG1, $MoSe_2$/NG2, $MoSe_2$/NG3, and $MoSe_2$/NG4 composites, respectively. Among them, $MoSe_2$/NG2 possesses the smallest Tafel slope, indicating the best HER activity. The results are in agreement with the above LSV analysis. Importantly, the Tafel slope can be used to distinguish the pathways of the reaction in the HER process in acidic electrolyte [44, 45]. In the primary discharge step, Volmer reaction occurs: $H_3O^+ + e^- \rightarrow H_{ads} + H_2O$, which is followed by either an electrochemical desorption step (Heyrovsky reaction): $H_{ads} + H_3O^+ + e^- \rightarrow H_2 + H_2O$, or a recombination step (Tafel reaction): $H_{ads} + H_{ads} \rightarrow H_2$. At the slope of about 120 mV dec^{-1}, Volmer reaction is indeed the rate-limiting process for HER, but Heyrovsky or Tafel reaction is the rate-limiting procedure at a Tafel slope of 40 and 30 mV dec^{-1}. According to the fitted data, Volmer reaction seems to be the rate-limiting process in pure $MoSe_2$ samples, but Volmer–Heyrovsky or Volmer–Tafel mechanism for $MoSe_2$/RGO and $MoSe_2$/NG composites. Obviously, the synergistic effect of RGO/NG and $MoSe_2$ changes the rate-limiting mechanism. For comparison, the HER performances of various MoS_2 and $MoSe_2$ related materials have been added in Table S2 (Electronic Supplementary Information). As compared to the reported results, the small overpotential and Tafel slope indicate good electro-catalytic activity for HER of the as-prepared $MoSe_2$/NG composites in this work.

The double-layer capacity, C_{dl}, is used to determine the electrochemically active surface area (ECSA) of catalyst. Figure 6c shows the C_{dl} calculated from the CV curves (Figure S2). The C_{dl} value of $MoSe_2$/RGO and $MoSe_2$/NG composites are substantially

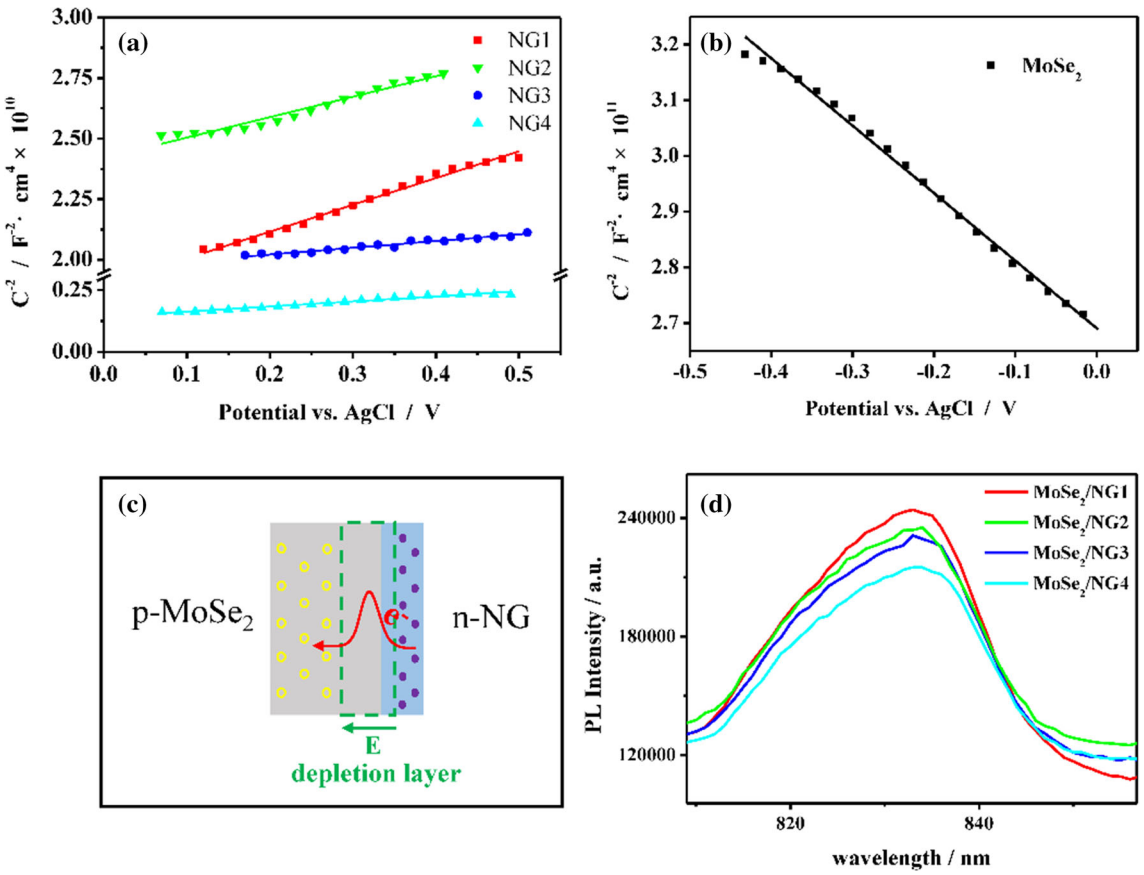

Figure 7 **a** Mott–Schottky curves of NG, **b** Mott–Schottky curves of pure $MoSe_2$, **c** Schematic diagram of depletion layer at interface between p-MoSe2 and n-NG, **d** PL spectrum of $MoSe_2$/NG.

increased as compared to pure $MoSe_2$, which can be ascribed to the dispersed $MoSe_2$ nanosheets and more active sites exposed, owing to the large specific surface area. So, they exhibit enhanced HER activity. Nearly the same C_{dl} in $MoSe_2$/RGO and $MoSe_2$/NG composites indicates no dependence of C_{dl} on the N/C ratio. Electrochemical impedance spectroscopy (EIS) is measured to study the reactions at the electrode/solution interface and the electron transfer kinetics in the HER process [42]. The Nyquist plots are displayed in Fig. 6d, and a facile Randle equivalent circuit is plotted in the inset of Fig. 6d to model the impedance data [46]. The values of R_s and charge transfer resistance (R_{ct}) are listed in Table 1. R_s is all about 1.5 Ω, and the low value indicates an intimate contact between catalysts and CFP substrate. The R_{ct} derived from the low frequency zone is related to the electro-catalytic kinetics at the interface between electro-catalysts and electrolyte, and a lower R_{ct} corresponds to a faster electron transfer [47]. As listed in Table 1, the $MoSe_2$/RGO and $MoSe_2$/NG composites have smaller R_{ct} than pure $MoSe_2$, among them, that of the $MoSe_2$/NG2 composite is the smallest one (6.82 Ω). So the electron transfer at electrode/solution interface in $MoSe_2$/NG2 is fastest, resulting in the best performance.

In fact, RGO and NG sheets have been adopted as the supports to improve the electro-catalytic HER activity. The good electrical conductivity of NG sheets makes it more effective than RGO. Figure 7a presents the Mott–Schottky curves. Accordingly, the carrier concentration in NG is fitted, and the results are listed in Table S3. The carrier concentration gradually increases with N/C ratio owing to more pyridinic-N-doped in NG, [32] and the activity of $MoSe_2$/NG should increase correspondingly. But the experimental results deviate from this trend slightly. As displayed in Fig. 7b, the slope of the Mott–Schottky curve of pure $MoSe_2$ is negative, characteristic of p-type feature. It changes from p-type to n-type upon N-doping, which is confirmed by the positive slope of Mott–Schottky curve of NG (Fig. 7a).

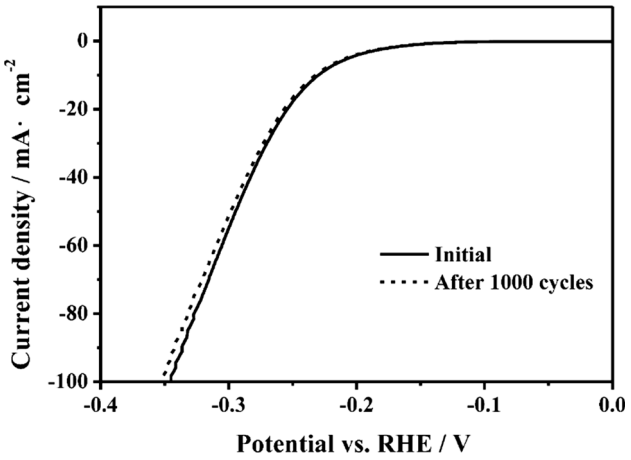

Figure 8 Stability tests of $MoSe_2$/NG2 samples.

A p–n junction might be formed when p-$MoSe_2$ is stacked on n-NG. So a narrow depletion layer emerges at the interface between $MoSe_2$ and NG (Fig. 7c), resulting in an energy barrier, which will block the electron transfer from NG to $MoSe_2$ during electrocatalytic HER process. PL spectra are measured to examine the change of energy barrier at interface. If the energy barrier is higher, the photo-induced electron and holes will be more effectively separated from each other and the intensity of PL peak will be lowered. As shown in Fig. 7d, the intensity of PL peak of $MoSe_2$/NG decreases with increasing N/C ratio gradually. It can be inferred that the energy barrier between $MoSe_2$ and NG increases with N/C ratio, namely, the electron transfer at interface is not efficient at high N/C ratio. So both the electrical conductivity of NG and the energy barrier at interface affect the HER activity. At low N/C ratio (1.13 and 1.94 at%), the activity of $MoSe_2$/NG increases with carrier concentration in NG because of negligible energy barrier and enhanced electron transfer. However, at high N/C ratio (3.0 and 5.16 at%), the energy barrier at interface will block the electron transfer from NG to $MoSe_2$ substantially so that the activity of $MoSe_2$/NG3 and $MoSe_2$/NG4 with high carrier concentration, on the contrary, is lowered as compared to $MoSe_2$/NG2. To assess the stability of $MoSe_2$/NG2 composites in the HER process, [48] continuous HER test for 1000 cycles are conducted. The polarization curves before and after 1000 cycles are shown in Fig. 8. The HER activity decreases only a little after 1000 cycles, so the stability of $MoSe_2$/NG2 in HER is good.

Conclusion

In summary, $MoSe_2$/NG composites are synthesized through a facile two-step hydrothermal approach. XPS, XRD, FESEM, TEM, and Raman spectra are adopted to characterize the structures and morphologies. In the composites, nanoclusters of $MoSe_2$ nanosheets are dispersed on plicated NG nanosheets. As the N/C ratio is increased, the plicated feature of NG becomes more remarkable, and the carrier concentration in NG increases gradually. The electrochemical measurement shows the synergistic effect of N-doping in RGO and $MoSe_2$ can greatly improve the activity for HER. The activity of $MoSe_2$/NG depends not only on the carrier concentration in NG but also on the interfacical energy barrier between $MoSe_2$ and NG. At low N/C ratio, the activity of $MoSe_2$/NG increases with carrier concentration in NG because of the negligible energy barrier and remarkable electron transfer. However, at high N/C ratio, the energy barrier becomes high enough to block the electron transfer substantially. Consequently, the highest activity can be obtained in $MoSe_2$/NG composites with an intermediate N/C ratio. It suggests us that an appropriate N-doping is indispensible to improve the HER activity of TMDs/RGO hybrid structures.

Acknowledgements

This work was jointly supported by National Natural Science Foundation of China (Grant Nos. 51471130, 51771144, 51501012, 51601142), Natural Science Foundation of Shaanxi Province (No.2017JZ015),the fund of the State Key Laboratory of Solidification Processing in NWPU (SKLSP201708), and Fundamental Research Funds for the Central Universities.

Electronic supplementary material: The online version of this article (doi:10.1007/s10853-017-1417-7) contains supplementary material, which is available to authorized users.

References

[1] Zhuang M, Ou X, Dou Y et al (2016) Polymer-embedded fabrication of Co2P nanoparticles encapsulated in N, P-doped graphene for hydrogen generation. Nano Lett 16:4691–4698. doi:10.1021/acs.nanolett.6b02203

[2] Xie J, Zhang H, Li S et al (2013) Defect-rich MoS_2 ultrathin nanosheets with additional active edge sites for enhanced electrocatalytic hydrogen evolution. Adv Mater 25:5807–5813. doi:10.1002/adma.201302685

[3] An L, Huang L, Zhou P, Yin J, Liu H, Xi P (2015) A self-standing high-performance hydrogen evolution electrode with nanostructured $NiCo_2O_4$/CuS heterostructures. Adv Funct Mater 25:6814–6822. doi:10.1002/adfm.201503784

[4] Zhou W, Lu J, Zhou K et al (2016) $CoSe_2$ nanoparticles embedded defective carbon nanotubes derived from MOFs as efficient electrocatalyst for hydrogen evolution reaction. Nano Energy 28:143–150. doi:10.1016/j.nanoen.2016.08.040

[5] Zhong X, Sun Y, Chen X, Zhuang G, Li X, Wang J-G (2016) Mo doping induced more active sites in urchin-like $W_{18}O_{49}$ nanostructure with remarkably enhanced performance for hydrogen evolution reaction. Adv Funct Mater 26:5778–5786. doi:10.1002/adfm.201601732

[6] Dai X, Li Z, Du K et al (2015) Facile synthesis of in–situ nitrogenated graphene decorated by few-layer MoS2 for hydrogen evolution reaction. Electrochim Acta 171:72–80. doi:10.1016/j.electacta.2015.05.017

[7] Kong D, Wang H, Lu Z, Cui Y (2014) $CoSe_2$ nanoparticles grown on carbon fiber paper: an efficient and stable electrocatalyst for hydrogen evolution reaction. JACS 136:4897–4900. doi:10.1021/ja501497n

[8] Zhang Y, Zuo L, Zhang L et al (2016) Cotton wool derived carbon fiber aerogel supported few-layered $MoSe_2$ nanosheets as efficient electrocatalysts for hydrogen evolution. ACS Appl Mater Interfaces 8:7077–7085. doi:10.1021/acsami.5b12772

[9] Zhang Y, Chang TR, Zhou B et al (2014) Direct observation of the transition from indirect to direct bandgap in atomically thin epitaxial $MoSe_2$. Nat Nanotechnol 9:111–115. doi:10.1038/nnano.2013.277

[10] Tang H, Dou KP, Kaun CC, Kuang Q, Yang SH (2014) $MoSe_2$ nanosheets and their graphene hybrids: synthesis, characterization and hydrogen evolution reaction studies. J Mater Chem A 2:360–364. doi:10.1039/C3ta13584e

[11] Larentis S, Fallahazad B, Tutuc E (2012) Field-effect transistors and intrinsic mobility in ultra-thin $MoSe_2$ layers. Appl Phys Lett 101:223104. doi:10.1063/1.4768218

[12] Xia J, Huang X, Liu L-Z et al (2014) CVD synthesis of large-area, highly crystalline $MoSe_2$ atomic layers on diverse substrates and application to photodetectors. Nanoscale 6:8949–8955. doi:10.1039/c4nr02311k

[13] Shim GW, Yoo K, Seo S-B et al (2014) Large-area single-layer $MoSe_2$ and its van der Waals heterostructures. ACS Nano 8:6655–6662. doi:10.1021/nn405685j

[14] Lei Z, Xu S, Wu P (2016) Ultra-thin and porous $MoSe_2$ nanosheets: facile preparation and enhanced electrocatalytic activity towards the hydrogen evolution reaction. PCCP 18:70–74

[15] Xu C, Peng S, Tan C et al (2014) Ultrathin S-doped $MoSe_2$ nanosheets for efficient hydrogen evolution. J Mater Chem A 2:5597–5601. doi:10.1039/c4ta00458b

[16] Gong Q, Cheng L, Liu C et al (2015) Ultrathin $MoS_{2(1-x)}Se_{2x}$ alloy nanoflakes for electrocatalytic hydrogen evolution reaction. ACS Catal 5:2213–2219. doi:10.1021/cs501970w

[17] Gupta U, Naidu BS, Maitra U et al (2014) Characterization of few-layer 1T-$MoSe_2$ and its superior performance in the visible-light induced hydrogen evolution reaction. APL Mater 2:092802. doi:10.1063/1.4892976

[18] Yuan HY, Li JY, Yuan C, He Z (2014) Facile synthesis of MoS_2@CNT as an effective catalyst for hydrogen production in microbial electrolysis cells. Chemelectrochem 1:1828–1833. doi:10.1002/celc.201402150

[19] Liao L, Zhu J, Bian X et al (2013) MoS_2 formed on mesoporous graphene as a highly active catalyst for hydrogen evolution. Adv Funct Mater 23:5326–5333. doi:10.1002/adfm.201300318

[20] Gopalakrishnan K, Pramoda K, Maitra U, Mahima U, Shah MA, Rao CNR (2015) Performance of MoS_2-reduced graphene oxide nanocomposites in supercapacitors and in oxygen reduction reaction. Nanomater Energy 4:9–17. doi:10.1680/nme.14.00024

[21] Ma C-B, Qi X, Chen B et al (2014) MoS_2 nanoflower-decorated reduced graphene oxide paper for high-performance hydrogen evolution reaction. Nanoscale 6:5624–5629

[22] Zhang Z, Lu B, Hao J, Yang W, Tang J (2014) FeP nanoparticles grown on graphene sheets as highly active non-precious-metal electrocatalysts for hydrogen evolution reaction. Chem Commun 50:11554–11557

[23] Pramoda K, Gupta U, Ahmad I, Kumar R, Rao CNR (2016) Assemblies of covalently cross-linked nanosheets of MoS_2 and of MoS_2–RGO: synthesis and novel properties. J Mater Chem A 4:8989–8994. doi:10.1039/c6ta00645k

[24] Zhong J, Deng J-J, Mao B-H et al (2012) Probing solid state N-doping in graphene by X-ray absorption near-edge structure spectroscopy. Carbon 50:335–338. doi:10.1016/j.carbon.2011.08.046

[25] Pan Y, Yang N, Chen Y et al (2015) Nickel phosphide nanoparticles-nitrogen-doped graphene hybrid as an efficient catalyst for enhanced hydrogen evolution activity. J Power Sources 297:45–52. doi:10.1016/j.jpowsour.2015.07.077

[26] Gopalakrishnan K, Rao CNR (2015) Remarkable performance of heavily nitrogenated graphene in the oxygen reduction reaction of fuel cells in alkaline medium. Mater Res Exp 2:095503. doi:10.1088/2053-1591/2/9/095503

[27] Jia L, Wang D-H, Huang Y-X, Xu A-W, Yu H-Q (2011) Highly durable N-Doped graphene/CdS nanocomposites with enhanced photocatalytic hydrogen evolution from water under visible light irradiation. J Phys Chem C 115:11466–11473. doi:10.1021/jp2023617

[28] Huang Z, Lv C, Chen Z, Chen Z, Tian F, Zhang C (2015) One-pot synthesis of diiron phosphide/nitrogen-doped graphene nanocomposite for effective hydrogen generation. Nano Energy 12:666–674

[29] Zhao K, Gu W, Zhao L, Zhang C, Peng W, Xian Y (2015) MoS_2/Nitrogen-doped graphene as efficient electrocatalyst for oxygen reduction reaction. Electrochim Acta 169:142–149. doi:10.1016/j.electacta.2015.04.044

[30] Hummers WS, Offeman RE (1958) Preparation of graphitic oxide. JACS 80:1339. doi:10.1021/ja01539a017

[31] Du C, Huang H, Feng X, Wu S, Song W (2015) Confining MoS_2 nanodots in 3D porous nitrogen-doped graphene with amendable ORR performance. J Mater Chem A 3:7616–7622. doi:10.1039/c5ta00648a

[32] Ma J, Habrioux A, Luo Y et al (2015) Electronic interaction between platinum nanoparticles and nitrogen-doped reduced graphene oxide: effect on the oxygen reduction reaction. J Mater Chem A 3:11891–11904. doi:10.1039/c5ta01285f

[33] Mao S, Wen ZH, Ci SQ, Guo XR, Ostrikov K, Chen JH (2015) Perpendicularly oriented $MoSe_2$/graphene nanosheets as advanced electrocatalysts for hydrogen evolution. Small 11:414–419. doi:10.1002/smll.201401598

[34] Chang K, Mei Z, Wang T, Kang Q, Ouyang S, Ye J (2014) MoS_2/graphene cocatalyst for efficient photocatalytic H_2 evolution under visible light irradiation. ACS Nano 8:7078–7087. doi:10.1021/nn5019945

[35] Kong DS, Wang HT, Cha JJ et al (2013) Synthesis of MoS_2 and $MoSe_2$ films with vertically aligned layers. Nano Lett 13:1341–1347. doi:10.1021/Nl400258t

[36] Zhang L, Sun L, Liu S, Huang YH, Xu KW, Ma F (2016) Effective charge separation and enhanced photocatalytic activity by the heterointerface in MoS_2/reduced graphene oxide composites. RSC Adv 6:60318–60326. doi:10.1039/c6ra10923c

[37] Pham TT, Santos CN, Joucken F, Hackens B, Raskin J-P, Sporken R (2016) The role of SiC as a diffusion barrier in the formation of graphene on Si(111). Diam Relat Mater 66:141–148. doi:10.1016/j.diamond.2016.04.011

[38] He L, Jing L, Luan Y, Wang L, Fu H (2014) Enhanced visible activities of α-Fe_2O_3 by coupling N-doped graphene and mechanism insight. ACS Catal 4:990–998. doi:10.1021/cs401122e

[39] Iamprasertkun P, Krittayavathananon A, Sawangphruk M (2016) N-doped reduced graphene oxide aerogel coated on carboxyl-modified carbon fiber paper for high-performance ionic-liquid supercapacitors. Carbon 102:455–461. doi:10.1016/j.carbon.2015.12.092

[40] Wang C, Kang J, Sun H, Ang HM, Tade MO, Wang S (2016) One-pot synthesis of N-doped graphene for metal-free advanced oxidation processes. Carbon 102:279–287. doi:10.1016/j.carbon.2016.02.048

[41] Asedegbega-Nieto E, Perez-Cadenas M, Morales MV et al (2014) High nitrogen doped graphenes and their applicability as basic catalysts. Diam Relat Mater 44:26–32. doi:10.1016/j.diamond.2014.01.019

[42] Huang J, Chen F, Zhang Q et al (2015) 3D silver nanoparticles decorated zinc oxide/silicon heterostructured nanomace arrays as high-performance surface-enhanced raman scattering substrates. ACS Appl Mater Interfaces 7:5725–5735. doi:10.1021/am507857x

[43] Wang K, Xi D, Zhou C et al (2015) $CoSe_2$ necklace-like nanowires supported by carbon fiber paper: a 3D integrated electrode for the hydrogen evolution reaction. J Mater Chem A 3:9415–9420. doi:10.1039/c5ta01143d

[44] Conway BE, Tilak BV (2002) Interfacial processes involving electrocatalytic evolution and oxidation of H_2, and the role of chemisorbed H. Electrochim Acta 47:3571–3594. doi:10.1016/S0013-4686(02)00329-8

[45] Li Y, Wang H, Xie L, Liang Y, Hong G, Dai H (2011) MoS_2 nanoparticles grown on graphene: an advanced catalyst for the hydrogen evolution reaction. JACS 133:7296–7299. doi:10.1021/ja201269b

[46] Chen X, Liu G, Zheng W et al (2016) Vertical 2D MoO_2/$MoSe_2$ core-shell nanosheet arrays as high-performance electrocatalysts for hydrogen evolution reaction. Adv Funct Mater 26:8537–8544. doi:10.1002/adfm.201603674

[47] Wang K, Ye Z, Liu C et al (2016) Morphology-controllable synthesis of cobalt telluride branched nanostructures on carbon fiber paper as electrocatalysts for hydrogen evolution reaction. ACS Appl Mater Interfaces 8:2910–2916. doi:10.1021/acsami.5b10835

[48] Zhou H, Yu F, Huang Y et al (2016) Efficient hydrogen evolution by ternary molybdenum sulfoselenide particles on self-standing porous nickel diselenide foam. Nat Commun 7:12765. doi:10.1038/ncomms12765